PAPER

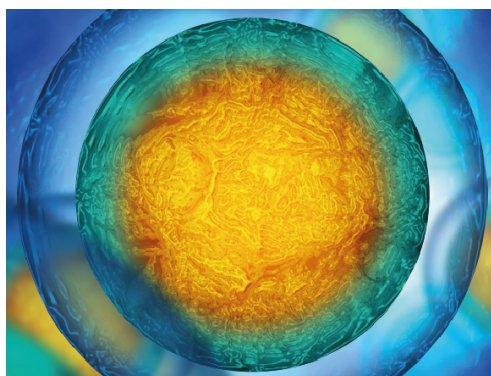# Hydrodynamic investigation of a self-propelled robotic fish based on a force-feedback control method

View the article online for updates and enhancements.

Related content

- Hydrodynamics of a robotic fish tail: effects of the caudal peduncle, fin ray motions and the flow speed
  Ziyu Ren, Xingbang Yang, Tianmiao Wang et al.

- Hydrodynamic performance of a biomimetic robotic swimmer actuated by ionic polymer–metal composite
  Qi Shen, Tiammiao Wang, Jianhong Liang et al.

- Self-propelled swimming simulations of bio-inspired smart structures
  Mohsen Daghooghi and Iman Borazjani

Recent citations

- Hydrodynamics of Biomimetic Marine Propulsion and Trends in Computational Simulations
  M. I. Lamas and C. G. Rodriguez

- Junzhi Yu and Min Tan

- Bottom-level motion control for robotic fish to swim in groups: modeling and experiments
  Liang Li *et al*

Hydrodynamic investigation of a self-propelled robotic fish based on a force-feedback control method

L Wen[1], T M Wang[2], G H Wu[3] and J H Liang[2]

[1] Museum of Comparative Zoology, Harvard University, 26 Oxford Street, Cambridge, MA 02138, USA
[2] Robotic Institute in School of Mechanical Engineering and Automation, Beihang University, Beijing 100191, People's Republic of China
[3] State Key Laboratory of Precision Measurement Technology and Instruments, Department of Precision Instruments, Tsinghua University, Beijing 100084, People's Republic of China

E-mail: liwen@oeb.harvard.edu

Abstract

We implement a mackerel (*Scomber scombrus*) body-shaped robot, programmed to display the three most typical body/caudal fin undulatory kinematics (i.e. anguilliform, carangiform and thunniform), in order to biomimetically investigate hydrodynamic issues not easily tackled experimentally with live fish. The robotic mackerel, mounted on a servo towing system and initially at rest, can determine its self-propelled speed by measuring the external force acting upon it and allowing for the simultaneous measurement of power, flow field and self-propelled speed. Experimental results showed that the robotic swimmer with thunniform kinematics achieved a faster final swimming speed ($St = 0.424$) relative to those with carangiform ($St = 0.43$) and anguilliform kinematics ($St = 0.55$). The thrust efficiency, estimated from a digital particle image velocimetry (DPIV) flow field, showed that the robotic swimmer with thunniform kinematics is more efficient (47.3%) than those with carangiform (31.4%) and anguilliform kinematics (26.6%). Furthermore, the DPIV measurements illustrate that the large-scale characteristics of the flow pattern generated by the robotic swimmer with both anguilliform and carangiform kinematics were wedge-like, double-row wake structures. Additionally, a typical single-row reverse Karman vortex was produced by the robotic swimmer using thunniform kinematics. Finally, we discuss this novel force-feedback-controlled experimental method, and review the relative self-propelled hydrodynamic results of the robot when utilizing the three types of undulatory kinematics.

(Some figures may appear in colour only in the online journal)

1. Introduction

Fish species that primarily use body/caudal fin (BCF) undulation for propulsion, such as eels, tuna and mackerel, display diverse sizes, shapes and kinematics [1]. Eels, mackerel and tuna, termed anguilliform, carangiform and thunniform swimmers, respectively, are the three most typical types of BCF species, and significantly differ in both kinematics and hydrodynamics [2, 3]. Thrust efficiency and self-propelled swimming speed are commonly considered the

most important metrics for the design criteria of a man-made machine, and inspiration from biological studies has already shed much light on many engineering designs. Robots with different 'morphologies' have been developed to move with specific kinematics based upon data derived directly from the observation of live swimmers. For instance, Hultmark *et al* [4] investigated the hydrodynamic performance of an anguilliform robotic swimmer using kinetic parameters obtained from live American eels (*Anguilla rostrata*). Yu *et al* [5] and Brenden *et al* [6] similarly implemented carangiform

1

robotic swimmers based on kinematics data drawn from observations of swimming mackerel (*Scomber scombrus*). The robotic thunniform swimmer, designed by Barrett *et al* [7] and Anderson and Chhabra [8], employed the kinematics data obtained from observing live yellow-fin tunas (*Thunnus albacares*). Whether using speed or thrust efficiency as a metric, however, robotic fish still lag behind their live counterparts [6–10].

As documented by Breder [3], anguilliform, carangiform and thunniform swimmers follow their own specific patterns of movement. Occasionally, however, biologists have found evidence of so-called hybrid kinematics within the standard patterns of undulatory locomotion. For example, Liao found that needlefish (*Belonidae*) [11], although possessing slender anguilliform bodies, use a carangiform swimming mode. Lighthill [12] suggested that large-amplitude undulations occur along the entire body of eels, but recent data provided by Tytell and Lauder [13] indicated that the anterior body (30%–40% of the body length) of eels only begins to undulate at very high swimming speeds or under fast acceleration. The undulation is confined to the posterior region at relatively lower speeds as in carangiform swimmers, somewhat different from the typical anguilliform kinematics reported by Lighthill. Additionally, leopard sharks (*Triakis semifasciata*) and bamboo sharks (*Chiloscyllium punctatum*) are defined as carangiform species, but at times have been observed to swim using very flexible body undulations like anguilliform swimmers [14]. Although these aforementioned experiments only focus on kinematic exceptions in some fish species, their results are interesting and possibly useful for a better understanding of undulatory locomotion.

As suggested by biologists' recent papers [15, 16], biomimetic robots offer many experimental advantages over their live counterparts: the ability to precisely control movement, accurately measure hydrodynamic forces and to explore a range of kinematics broader than that which exists in nature, including movement patterns that are not commonly used by live swimmers. In this experiment, we employ a biomimetic robotic fish using the three most typical BCF undulatory kinematics to investigate the hydrodynamic effects of each movement pattern.

Understanding how the different kinematics of an aquatic animal affects its overall thrust performance requires qualitative hydrodynamic experimentation. At the same time, comparing the robotic mackerel's thrust performance with these three kinematic modes requires serious attention to the robot's physical configuration; i.e. the swimming of the robotic fish should be performed under self-propelled rather than tethered conditions. Without self-propulsion, the excess thrust force generated by the swimming will be absorbed by external connectors such as the streamlined strut [7, 17, 18], steel wire [19], etc. In this case, the self-propelled speed for each distinct kinematic mode cannot be accurately and scientifically ascertained. In this study, we propose a novel experimental method through which the robotic fish can vary its self-propelled speed based upon feedback of the measured external force of the swimming robotic fish. More specifically, the robotic fish was observed performing in a water tank:

initially at rest, then beginning to undulate its body using one of the three typical kinematics, and finally increasing its self-propelled swimming speed until the mean net axial force acting on the robotic fish reached zero. Thereafter, the robotic fish reached a steady swimming state under which the thrust performance of kinematic mode could be recorded and quantified. The hydrodynamic thrust performance was assessed under self-propelled conditions by simultaneously measuring power, external force, resulting wake structures and thrust efficiency through the force-feedback experimental method. To quantify the flow generated by the robotic fish, high-resolution digital particle image velocimetry (DPIV) was used. Furthermore, the results presented will be analyzed to elucidate several important aspects of fish locomotion and hydrodynamics.

## 2. Materials and methods

2.1. Force-feedback method for determining the robotic swimmer's self-propulsion

Before describing the experimental method of realizing self-propulsion, we review and summarize the two main conventional experimental approaches to a robotic swimmer in figure 1. As shown in figure 1(*a*), the robotic model is attached to a strut which holds the model vertically from the towing carriage above [7, 20], or is fixed in the circulating water tunnel by external connectors [19, 21]. Power and external forces can be measured by the transducers when the model is actively towed at a preset speed or is subjected to an oncoming flow velocity. In most other experiments, however, the robotic fish was not self-propelled and moved through the constrained, imposed flow; the thrust and drag forces were not equal. As most previous hydrodynamic research shows, the fish's speed, power consumption and wake structure came about through a similarly constrained approach [17].

In figure 1(*b*) the robotic fish undulates its body to create an axial force that induces passive speed on a low-friction air-bearing guide rail, where the thrust force equals the robotic model's unsteady drag coupled with the strut drag force (denoted by D_s in figure 1(*b*)). This method almost seems to satisfy the self-propelled condition; however, the passive towing system has two main defects. First, the additional parts as shown in figure 1 (e.g. slide block, strut, etc), which cannot be ignored, increase the additional inertial mass of the robotic fish model. Consequently, the acceleration of the robotic fish would be very different from a real situation with a live fish. Meanwhile, the self-propelled speed would be less accurate if other instruments (such as the DPIV and electronic facilities) were mounted on the air-bearing guide rail. Second, the towing system no longer has the capacity to provide a preset speed to actively tow the robotic model. This is inconvenient in measuring some quantitative hydrodynamic parameters, such as the drag coefficient of the robotic model.

Taking both the active and passive towing methods into consideration, we propose a novel experimental approach (see figure 1(*c*)) based on a force-feedback control technique which combines the advantages of both methods shown in figures 1(*a*)
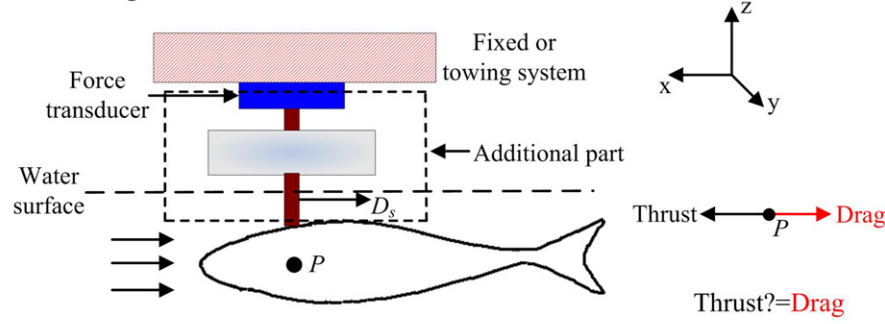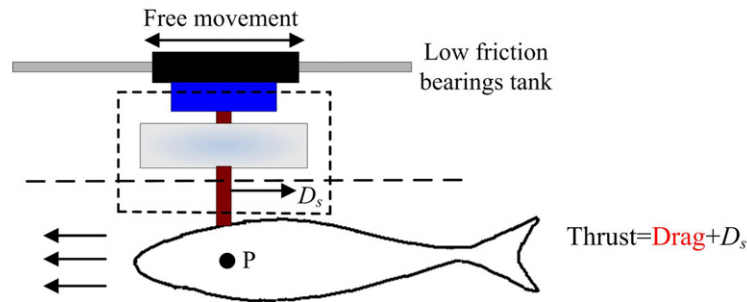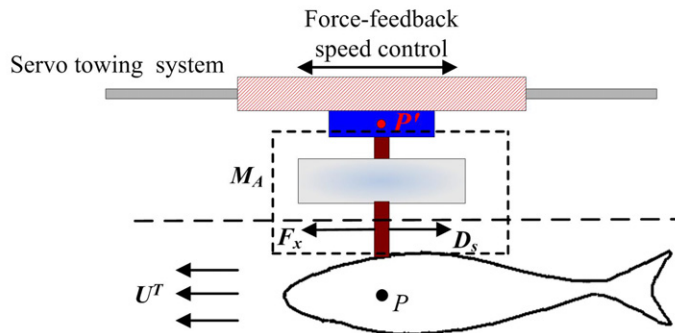
Figure 1. A schematic view illustrating the two conventional categories of hydrodynamic methods for the robotic model. (*a*) Active towing method: *P* denotes the robotic fish center of mass; *U* denotes the flow speed. (*b*) The passive towing method, where the robotic fish is free to move upstream and downstream on a low-friction air-bearing system. (*c*) The self-propelled method. The *x*-axis is along the fish axial length, the *y*-axis is in the lateral direction and the *z*-axis is selected to be orthogonal to the horizontal plane.

and (*b*). The mechanism of the self-propelled fish's undulating body in a medium is determined by the interaction of the fish's body movement with the varying fluid dynamics. From Newton's law, equations for the fish in the axial direction will satisfy

$$F_x = m \frac{\mathrm{d}U}{\mathrm{d}t}, \qquad (1)$$

where F_x denotes the net axial force of a freely swimming robotic fish. For a robotic model fixed under the towing system, as shown in figure 1(*c*), the force about the center of the multi-component force transducer (expressed by P') will satisfy the following:

$$F_x + F_{sx} + D_s = (m + m_A) \frac{\mathrm{d}U^T}{\mathrm{d}t}, \qquad (2)$$

where $F_{sx}(t)$ denotes the measured axial force and m_A denotes the mass of the additional parts under the force sensor

excluding the robotic fish, represented by the dashed box in figure 1(*c*). The mass of the additional parts in the current apparatus includes the following: the inherent mass of the multi-component force transducer, the mass of the robotic fish's actuators, the mechanical transmission system and the streamlined strut, which penetrates the water to connect to the robotic fish's head. U^T represents the axial speed of point P'. As the force transducer is fixed firmly to the towing system, U^T also denotes the forward speed of the towing system.

Equation (1) represents the self-propelled condition of the robotic fish in the axial direction. To make the robotic model swim with the self-propelled speed of a freely swimming fish, the speed of the towing system U^T should equal speed U of the self-propelled fish in equation (1) ($U = U^T$). Since the self-propelled speeds U and U^T satisfy the conditions of continuity

and differentiability, we obtain $dU^T/dt = dU/dt$. Combining $dU^T/dt = dU/dt$ with (1) and (2) gives

$$\frac{dU^T}{dt} = \frac{dU}{dt} = \left(\frac{F_{sx} + D_s}{m_A} \right). \tag{3}$$

With equation (3), the following coupled dynamic processes appear: (1) the fish's body undulates following certain kinematic movements, and the robotic fish moves starting from rest (the initial towing speed is zero), i.e. $U^T(0) = 0$; (2) the net axial force F_{sx} is measured by the multi-component force transducer while the robotic fish is undulating and (3) the towing speed U^T is calculated by the measured axial force according to equation (3). In such a situation, the robotic model will not be influenced by the constraining effects of the towing system, just as if the robotic fish were freely swimming in the axial direction. Even a small change in F_{sx} will be fed back, corresponding to a change in U^T by the towing system. We then represent (3) by the time-discrete form:

$$[U^T(t) - U^T(t - \Delta t)]/\Delta t = \frac{F_{sx}(t) + D_s}{m_A}. \tag{4}$$

Rather than using the newly measured instantaneous force in (4), a weighted average filtered force $F'_{sx}(t)$ is used instead as derived by the following:

$$F'_{sx}(t) = \sigma F_{sx}(t) + (1 - \sigma)F_{sx}(t - \Delta t), \tag{5}$$

where σ is the weighting factor. Tests showed that the optimal value for the current experimental apparatus for σ is 0.85; values below 0.85 make the whole towing system unstable and cause waking, whereas increasing σ from 0.85 to 1 reduces the accuracy of the force-feedback speed. Using the weighted average filtered force as given in (5), the towing speed in (4) can be rearranged into the following:

$$U^T(t) - U^T(t - \Delta t) = \left(\frac{F'_{sx}(t) + D_s}{m_A} \right) \Delta t. \tag{6}$$

The filtered axial force $F'_{sx}(t)$ will be fed back to determine the towing speed based on (6). As described above, the laboratory robotic fish fixed on a towing system can work under self-propelled conditions. As we use a low-drag streamlined strut that penetrates the water and connects to the head of the fish, the strut drag force D_s will be ignored. We currently only consider the lateral and rotational direction constraints on the fish's swimming and also did not consider the three-dimensional movement of the whole fish's body [22]. This simplified treatment was applied in this study because it has also been widely employed in many previous experimental and numerical hydrodynamic investigations [23–26].

2.2. Experimental self-propelled towing system and robotic fish apparatus

This section details our implementation of the self-propelled experimental apparatus, which includes the towing system and the robotic fish model. Figure 2 shows the experimental apparatus. The servo towing system is driven by a 4000 watt ac motor, has a travel distance of 7.5 m, a position accuracy of 0.1 mm and a maximum speed of 3 ms^{-1}. Underneath the towing system is a water tank measuring 7.8 m × 1.2 m × 1.1 m, in which the robotic fish has sufficient

Table 1. A comparison of body shape and mass between the live mackerel and the robotic fish.

Variable	Mackerel	Robotic fish	Difference
Caudal span ($/L$)	0.24	0.238	0.8%
Body volume (L^3)	0.0113	0.011 25	4.5%
Wetted area (L^2)	0.401	0.395	2%
Mass (kg)	2.68	2.79	4.1%

space to move. Furthermore, the robotic fish can move at mid-depth in the tank to avoid the interference effect of the free surface and the bottom of the tank. As figure 2(*a*) shows, the robotic fish and its mechanical transmission component are fixed under the force transducer. A low-drag streamlined strut penetrates the water and connects to the head of the fish. The external force of a robotic fish can be measured using a multi-component piezoelectric force transducer Kislter 9254C (Kislter Inc., Switzerland). The force transducer can be used for the robotic fish to determine its self-propelled speed (see equation (3) for notation). The output of the external Kislter transducer is also recorded by computer I (as shown in figure 2(*a*)) through a data cable using a Controller Area Network bus.

The DPIV system is used to measure the flow field. The image data are transferred through another cable to computer II for analysis, making it capable of capturing the particle images behind the robotic fish. As shown in the dashed blue box in figure 2(*a*), when the experimental apparatus was operational we were able to simultaneously run the power measurement system, DPIV system, force transducers mounted on the carriage running in the axial direction (with a speed denoted by U) and the movement of the robotic mackerel. More details of the DPIV apparatus, including the laser system, high-speed camera and the particles that seed into the water, have also been previously discussed in Wu *et al*'s live fish study [29]. A snapshot of the apparatus in operation is provided in figure 2(*b*). The computer-generated model of the robotic fish, which has a total length of 58.8 cm and 2.79 kg, shows that the robot is a relatively accurate replica of a real mackerel (*Scomber scombrus*) [33]. Table 1 summarizes a comparison between the 'morphological' properties of the live swimmer and the robotic fish. Figure 3 provides a snapshot of the robotic fish's internal fabrication without the 'skin' and 'muscle tissue'.

Details of the robotic swimmer's fabrication have also been discussed previously [28]. The present robot is an improvement on the preliminary implementation, which could already accurately measure power consumption. The power of the robotic fish is obtained by subtracting the pure mechanical power from the total power consumed by the actuators (Maxon RE40, Maxon Motor Inc., Switzerland). Previous biological studies also indicated that this is the effective way to obtain the power consumed purely by the fluid [7]. The instantaneous total power into the motor can be denoted as $P_j(t) = M_j(t)\omega_j(t)$, where j indicates the discrete number of robotic fish body actuators, and $j = 1, \ldots, 4$ in this study. $\omega_j(t)$ denotes the angular speed of the motor at a certain instant, which is obtained through the differential value of $\theta_j(t)$ of
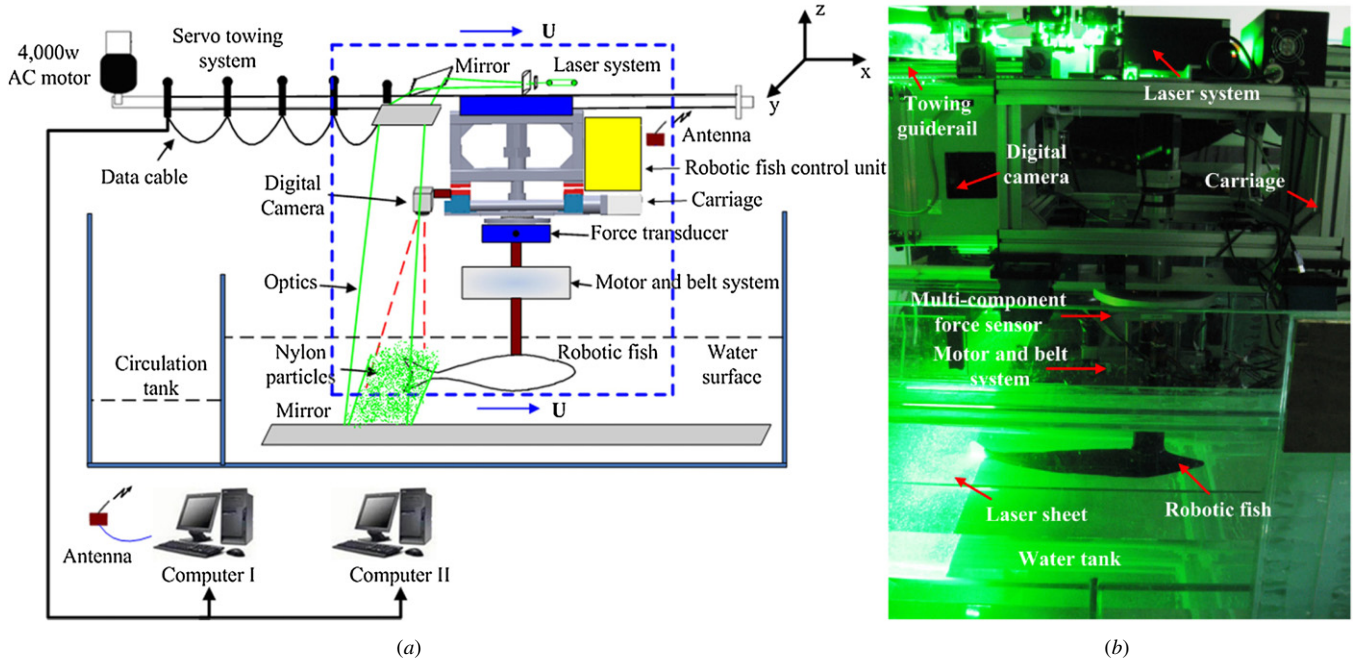
Figure 2. (*a*) A schematic view of the whole system for the self-propelled robotic fish model. Note that the box on the carriage represents the shelf for the robotic fish's power supply, motion control, amplifier and data acquisition system. The *x*-axis is along the fish axial length, the *y*-axis is in the lateral direction and the *z*-axis is selected to be orthogonal to the horizontal plane. (*b*) Snapshot of the experimental apparatus with the DPIV system in operation.
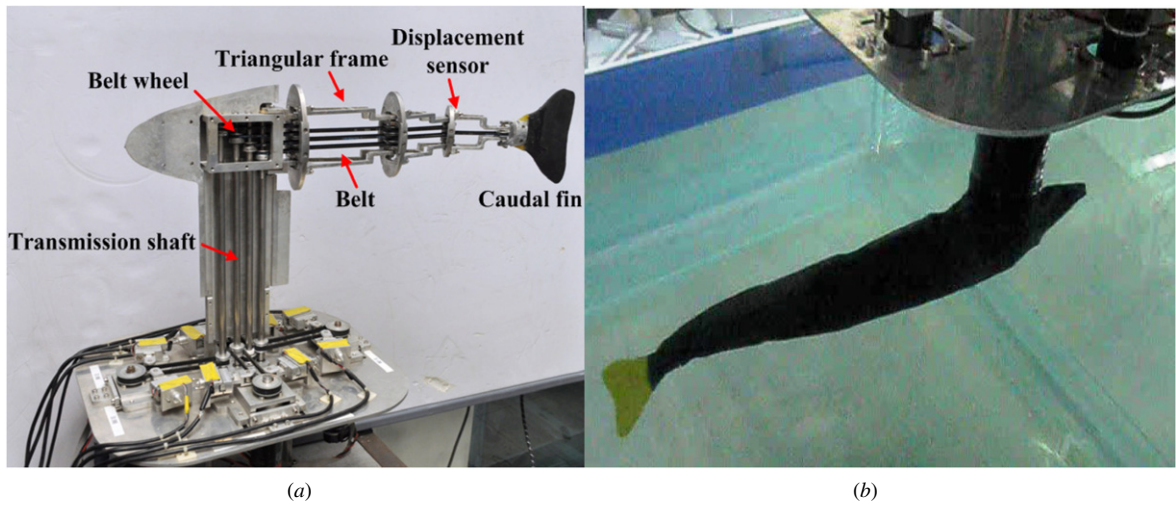

Figure 3. (*a*) A snapshot of the robotic model inside by removing the 'skin' and 'muscle tissue' (the robotic model is upside down). (*b*) A snapshot of the robotic fish model that is swimming in the water tank.

a potentiometer SV01A103 (Murata Manufacturing Co. Ltd, Japan) built into the fish rotation links, and $\omega_j(t) = \mathrm{d}(\theta_j(t))/\mathrm{d}t$. The torque constant K_M links the mechanical torque M_i with the electric current I_i: $M_j(t) = K_M(t)I_j(t)$; the electrical current is measured by a Hall effect-based linear current sensor ACS712 (Microsystems Inc., USA), where $K_M = 0.03$ Nm A^{-1} for Maxon RE40. The circuit was measured across the analogue input channels on the Trio-P325 data acquisition card (Trio Motion Technology, UK), with a sampling rate of 200 Hz. The total average power consumption of the fish's body within a period is given in equation (7), derived from the integration of the four distinct actuators:

$$P_T = \frac{\int_0^T \sum_{i=1}^{i=4} M_i(t)\omega_i(t)\,\mathrm{d}t}{T},\qquad(7)$$

where P_T denotes the measured total average power and T denotes the undulating period of the robotic fish. We obtained P_T and the mechanical transmission power P_M from when the robotic fish undulated in water and air, respectively. P_M was removed from the measured total average power to yield the pure fluid power:

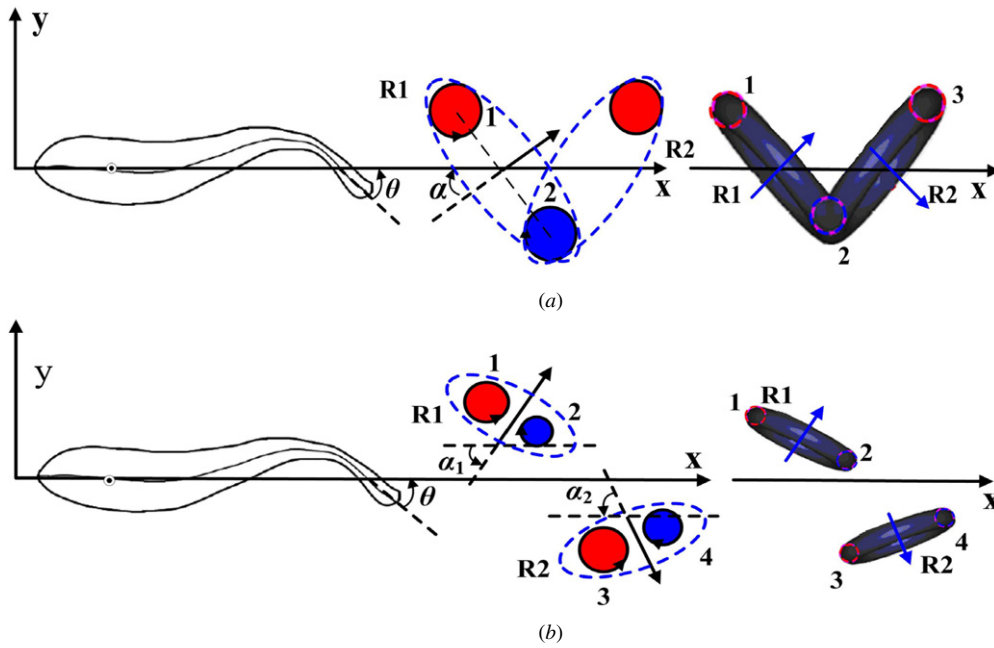$$P_{\text{fluid}} = P_T - P_M.\qquad(8)$$

Figure 4. Schematic views of (*a*) single-row and (*b*) double-row vortices. The different colors indicate the different directions of vortex rotation, and the arrows indicate the directions of the jet flow.

The DPIV system and associated open-source software toolbox [27] were used to measure the flow field generated by the robotic fish. In this paper, the two-dimensional vortex ring model, which assumes that all momentum created by the robotic fish is contained in elliptical vortex rings, is applied to estimate the thrust force. There are two main different types of wake structures generated by the robotic fish. Note that the formation of these two wake structures will be introduced later in section 3. For single-row vortices, as can be seen from figure 4(*a*), the vortex rings form a linked chain, and only one vortex ring (i.e. two vortices in the two-dimensional plane, which are denoted by vortices 1 and 2) was generated per flapping cycle. The total force was resolved geometrically using the jet angle α to determine the axial component of force. The time-averaged thrust force is denoted as T_f:

$$T_f = I f \cos \alpha, \tag{9}$$

where f denotes the flapping frequency of the robotic fish and I denotes the impulse of the vortex ring. For the double-row vortices, as can be seen from figure 4(*b*), the robotic fish generates two vortex rings (i.e. four vortices in the two-dimensional plane, which are denoted by vortices 1–4) per flapping cycle. The time-averaged thrust force T_f is

$$T_f = I_1 f \cos \alpha_1 + I_2 f \cos \alpha_2, \tag{10}$$

where α_1 and α_2 denote the jet angle of the two separated vortex rings for the case of a double-row wake structure. I_1 and I_2 denote each individual impulse of the vortex rings 1 and 2. Definitions and estimates of these parameters, along with vortex momentum, are described in Wu *et al*'s live fish study [29].

2.3. Anguilliform, carangiform and thunniform undulatory kinematics

How do we mathematically model the three distinct undulatory kinematic modes? First, body/caudal fin undulatory fish locomotion has been classified into three general types (anguilliform, carangiform and thunniform) based on experiments with live swimmers such as eels, mackerel and tuna [30]. Early biological studies [2, 3] defined two major criteria that distinguish the three kinematics: the percentage of the fish's body that undergoes undulatory movement, and the wavelength of the body during steady swimming. Fish and Lauder [32] also indicate that the caudal fin movement of most scombrid fishes (which includes the mackerel and tuna) does not simply function as a tangential extension of the body wave, but behaves as a distinct propeller like an oscillating foil with an adjustable pitch angle. Therefore, to construct models of the three kinematics, the undulatory swimming of a robotic mackerel is conceptualized as the movement of a waving body and an independent flapping caudal fin [33, 32]; the percentage of body undulation, body wavelength and caudal fin pitch angle are treated as principal parameters that differentiate the three undulatory kinematics.

First we consider the percentage of body undulation: Donley and Dickson [34] proposed that undulatory body movement occurs from 35%–40% L in mackerel and tuna, and suggested that thunniform locomotion is only a relatively modest variation of carangiform motion. Lighthill's classic paper [12] suggests that for eels, large-amplitude undulations occur along the entire body at all swimming speeds. Recent data provided by Tytell and Lauder [13], however, indicated that the anterior body (30%–40%) only begins undulating at very high swimming speeds or under fast acceleration, and that undulation is confined to the posterior region at relatively low speeds. Given that the anterior of the robotic swimmer's body
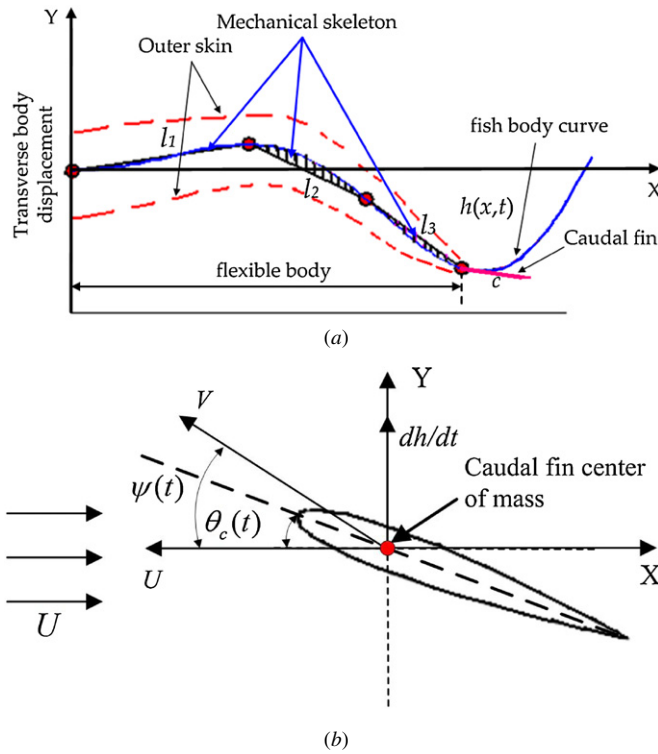
Figure 5. (*a*) A schematic view of the robotic mackerel and the mechanical links used to fit the curve of the fish kinematics. (*b*) Definition of the pitch angle $\theta_c(t)$ for the flapping caudal fin.

(roughly one third of its total body length) is mechanically rigid in this study, all undulatory movement for the three typical kinematics starts from one-third of the body length, measured from the nose of the robotic fish. Furthermore, it is important to point out that Shadwick and Lauder [30] stated that the body undulation profile at relatively low swimming speeds (less than 1.6–1.8 body lengths) is remarkably similar across all three kinematics [30]. Based on these findings, the posterior body parts (anterior to the caudal peduncle) of the present robotic model were programmed to swim, for all three kinematics, with the same wave equation:

$$h(x, t) = (c_1 x + c_2 x^2) \sin[kx \pm \omega t], \quad 0 < x \leqslant 2L/3 - c. \quad (11)$$

See figure 5(*a*) for notation: $h(x,t)$ denotes the displacement along the lateral direction in a body-fixed coordinate system; x denotes the displacement along the main body axis (note: x is measured starting from $1/3L$ of the robotic fish); L represents the total length of the robotic mackerel's body; c denotes the chord length of the caudal fin; $k = 2\pi/\lambda$ denotes the wave number, where λ is the body wavelength; ω denotes the circular frequency of oscillation and $\omega = 2\pi f$; c_1 and c_2 are applied and adjusted to achieve a specific value for the amplitude envelope of the body. Considering caudal fin motion, the heave and pitch motions of the tail at the caudal fin center of mass point can be defined as

$$\begin{cases} h_c = [h(x, t)]_{x=L-2c/3} \\ \theta_c = \theta_{max} \sin\left[\dfrac{2\pi}{\lambda}x \pm 2\pi f t + \psi\right]_{x=L-2c/3} \end{cases}, \quad (12)$$

where $h(x,t)$ again denotes the displacement along the lateral direction in a body-fixed coordinate system; h_c and θ_c denote

the heave and pitch motions, respectively; c denotes the chord length of the caudal fin; f represents the flapping frequency; ψ is the phase angle between the heave and the pitch motions; $x = L-2c/3$ denotes the position of the caudal fin center of mass, which connects the caudal peduncle; θ_{max} represents the pitch angle amplitude of the caudal fin [32].

According to Tytell and Lauder [13], the wavelength of typical anguilliform kinematics is 0.642 *L*. For carangiform swimmers, the wavelength is 0.95 *L*, in accordance with the mean propulsive wavelength of live mackerel, as reported by Hess and Videler [33]. The wavelength ($\lambda = 1.25L$) of the yellow-fin tuna reported by Dewar and Graham [35] is used for thunniform kinematics. Recall that caudal fin movement of anguilliform kinematics forms the angle tangent to the body wave at the point of conjunction [13]; see figure 5(*a*) for notation. The pitch angle of the caudal fin can be described as the angle between the line from the leading to the trailing edge of the artificial tail and the free stream flow (in the axial direction), clearly shown in figure 5(*b*). On the basis of the x-ray scan results of intervertebral bending angles of chub mackerel and kawakawa tuna by Donley and Dickson [34], the pitch angles are 20.5° and 11.5° for carangiform and thunniform kinematics, respectively, while a pitch angle of 26.5° is employed for anguilliform kinematics [13]. Therefore in this study, $\theta_{max} = 26.5°$, 20.5° and 11.5° for anguilliform, carangiform and thunniform kinematics, respectively. The above description accounts for a quantitative characterization of and a clear separation between the three distinct BCF kinematics. Moreover, all three kinematics have the same maximum displacement h_{max} at the caudal peduncle ($h_{max} = 0.1 L$), which is in accordance with the observed results of live swimmers [13, 33, 35].

Figures 6(*a*)–(*c*) show several ventral-view snapshots of the robotic mackerel in motion, where the posterior two-thirds of the body moves. Figures 6(*d*)–(*f*) show movement of the ventral-view midline of the robotic fish's body, digitized in Matlab by averaging five beat cycles. It should be noted that the body midline represents the oscillating part of the fish's body. Midlines at equally spaced time intervals throughout a tail beat can be observed; each time is shown in a distinct color. It can be observed that the movements of robotic fish are relevant to the kinematics of the live swimmer (more images of the body midlines of live fish can be found in figure 11.1 on page 427 of [30]). We compared the undulation amplitude of the actual midline motion curve at both the mid-body position ($x_1 = 195$ mm) and the caudal peduncle ($x_2 = 355$ mm). To provide a further quantitative assessment of the comparison values, the root-mean-square (RMS) error and the maximum error are used to measure differences between theoretical values predicted by the models and the actual values from observed results. In figure 6(*g*), both the RMS and the maximum errors of the midline lateral displacement are shown. The RMS and maximum errors of the body slope are also shown in figure 6(*h*). Note that the present RMS and maximum error values are the result of averaging five undulatory beat cycles.
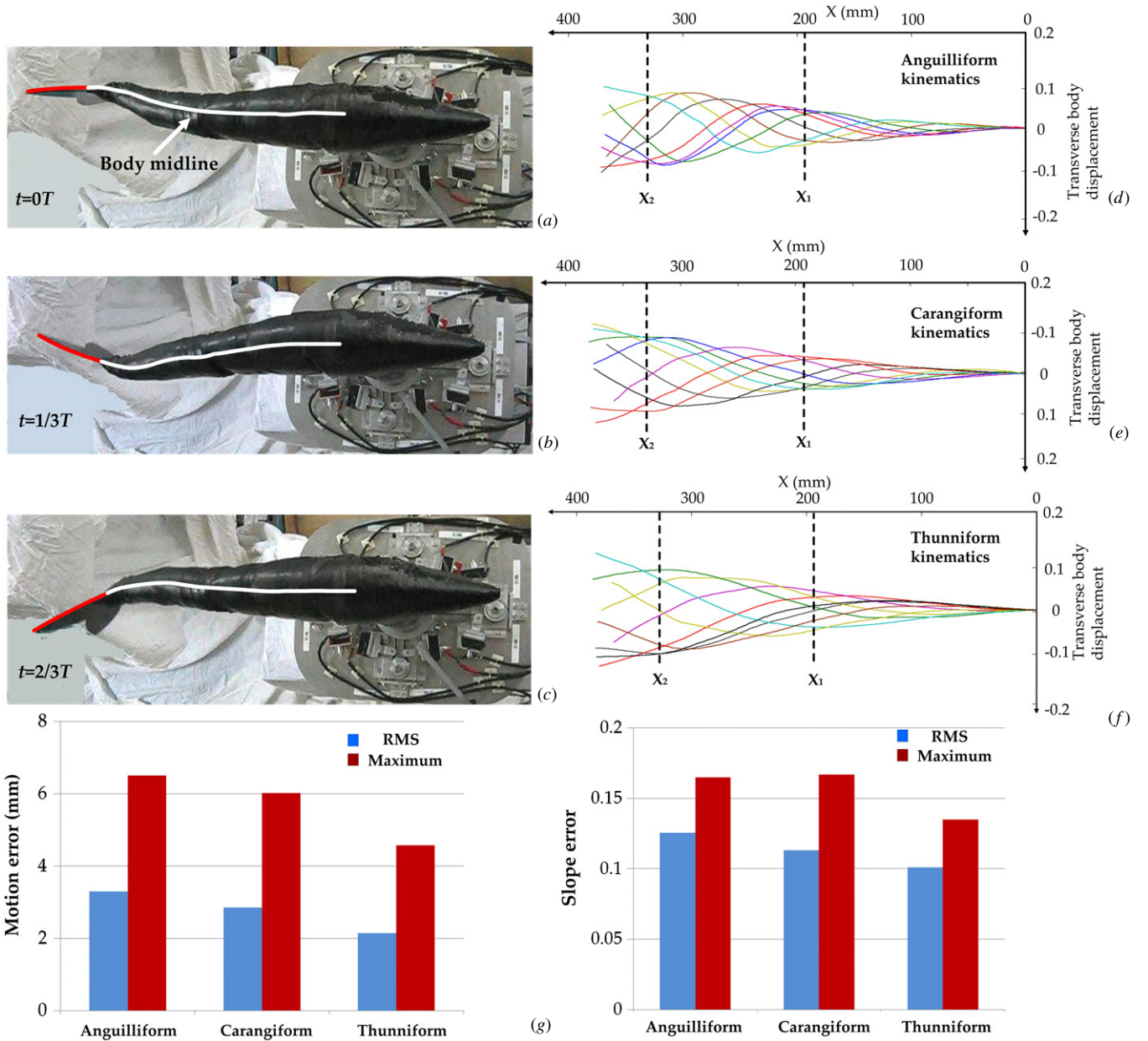
Figure 6. (*a*)–(*c*) Ventral views of the undulating robotic fish using carangiform kinematics at three instants for $f = 0.8$ Hz ($0T$, $T/3$, $2T/3$). The midline curves of the posterior two-thirds of the robotic fish's undulation with (*d*) anguilliform, (*e*) carangiform and (*f*) thunniform over one tail beat cycle. Two dashed lines represent the position of the mid-undulatory body ($x_1 = 195$ mm) and the caudal peduncle ($x_2 = 335$ mm), separately. (*g*) The RMS values of the motion errors, and the maximum errors of the body midline, both obtained by averaging five beat cycles. (*h*) The RMS of the slope errors, and the maximum slope errors of the body midline, both obtained by averaging five beat cycles.

2.4. Definitions of hydrodynamic dimensionless parameters

Conventionally, the thrust efficiency based on the thrust force for a constant swimming speed is defined by the following [12, 36]:

$$\eta = T_f U / P_{\text{fluid}}, \qquad (13)$$

where U denotes the self-propelled speed of the fish, T_f and P_{fluid} denote the time-averaged thrust and power which have already been defined in (9), (10) and (8). Note that force, speed, power consumption and flow field are necessary variables to qualify thrust efficiency [24]. The hydrodynamics of fish-like locomotion is dominated by the fundamental dimensionless parameter, the Strouhal number, defined as

$$St = \frac{2 f h_{\text{max}}}{U}, \qquad (14)$$

where h_{max} denotes the undulating amplitude of the caudal peduncle, defined as

$$h_{\text{max}} = |[h(x,t)]_{x=L}|_{\text{max}}, \qquad (15)$$

where $|\cdot|_{\text{max}}$ denotes the maximum absolute value; see (11) for the definition of $h(x,t)$ for notation. The thrust coefficient is defined as

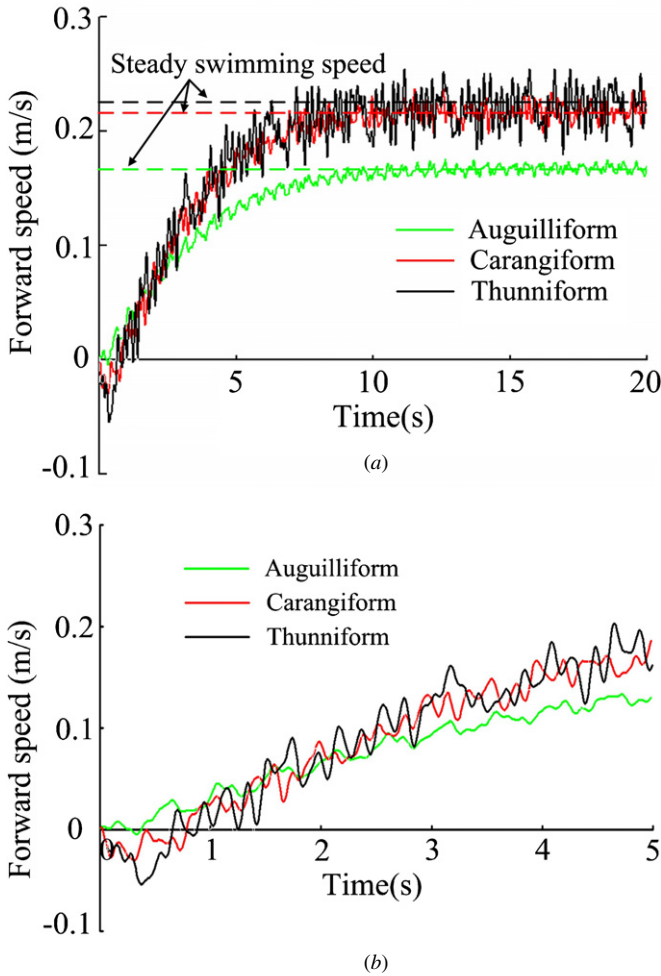$$C_T = \frac{T_f}{\rho U^2 L^2}, \qquad (16)$$

8

(a)

(b)

Figure 7. Self-propelled speed and force time history for hybrid kinematics. (*a*) Instantaneous speed. (*b*) Initial start phase of speed.
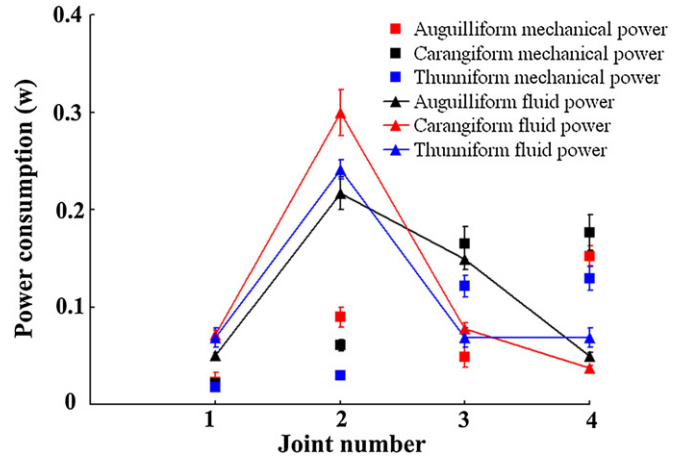

Figure 8. The mean power input to each joint for robotic fish with anguilliform, carangiform and thunniform kinematics under self-propelled conditions. 1–4 denote the number of discrete robotic fish body joints.

where ρ is the density of the fluid. The swimming power coefficient is defined as

$$C_p = \frac{P_{\text{fluid}}}{0.5\rho U^3 L^2},$$ (17)

where P_{fluid} denotes the average mean fluid power; see equation (8) for notation. Experimental uncertainties in the measured quantities are defined as the standard error of the mean [37]:

$$\bar{\sigma} = \sigma/\sqrt{N},$$ (18)

where σ is the sample standard deviation for each data point consisting of N measurements. In this study, $N = 5$. The error bars in figure 8 reflect the uncertainty.

3. Results

3.1. Self-propelled speed

First we demonstrate the speed results of the self-propelled robotic fish under the same fluid conditions (i.e. same water temperature of 20 °C and the same immersed depth for the fish's body). Three kinetic tests were performed with the same tail beat frequency ($f = 0.8$ Hz) and undulating amplitude ($h = 0.1$ L). The force-feedback control process was continued

for 20 s, a time duration long enough for the robotic swimmer to start from rest and reach a steady swimming state.

As can be observed from figure 7(*a*), during the initial 12 flapping beats of the robotic fish, all three cases resulted in a steady swimming state. Different steady swimming speeds were observed, and robotic fish with carangiform and thunniform kinematics reached a higher velocity, with the thunniform kinematics having a slight advantage over the carangiform. Considering the average speed in the steady states, as reported in table 2, the thunniform kinematics was 29.7% faster than the anguilliform, and 2% faster than the carangiform. We used the *St* as a metric of swimming hydrodynamic thrust performance of the robotic model, as defined previously. Recall that the lower the value of the *St* number, the faster the robotic fish swam for a given input flapping frequency and amplitude. The *St* values we obtained were 0.55, 0.43 and 0.424 for anguilliform, carangiform and thunniform kinematics, respectively. An interesting finding can be observed in figure 7(*b*): during the initial acceleration phase, the anguilliform robotic swimmer accelerated faster than the other two. In addition, the carangiform and thunniform swimmers initially had negative speeds; in comparison, the anguilliform had a positive speed throughout. Nevertheless, the swimmers using carangiform and thunniform kinematics overtook the anguilliform swimmer and ultimately performed better. This trend has also been documented in some experiments with live swimmers [39]; the literature suggests that fish might change their inherent movement pattern during the fast-start performance.

In this study, the average axial force over several cycles of undulatory movement was 0.003 N for auguilliform, 0.002 N for carangiform and 0.005 N for thunniform, demonstrating that the robotic fish satisfied the self-propelled condition while swimming. Although the average net forward force of the robotic fish was almost zero during a tail beat cycle at the steady swimming state, the force is not zero at every instant: the speed fluctuations might be due to the force oscillation within a tail beat cycle. Considering speed fluctuations in the axial direction, as can be seen from table 2,

Table 2. The kinematic and hydrodynamic results of the three undulatory kinematics.

Variable	Abbreviation	Anguilliform	Carangiform	Thunniform
Amplitude at $L/2$ (Theo)	–	0.0447	0.0447	0.0447
Amplitude at $L/2$ (Exp.)	–	0.0416	0.421	0.0410
Amplitude at $L/2$ (Theo)	–	0.1	0.1	0.1
Amplitude at $L/2$ (Exp.)	–	0.096	0.094	0.097
Speed (m s^{-1})	U	0.171	0.218	0.221
Strouhal number	St	0.55	0.43	0.424
Ratio of wave speed	δ	1.78	2.04	2.66
Power coefficient	C_p	0.003 24	0.003 39	0.0031
Speed fluctuations (m s^{-1})	r.m.s.	0.02	0.03	0.065
Angle of attack (°)	α	43.2	36.8	31.5
Jet angle (°)	γ	62.4	73.3	69.6
Vortex radius (mm)	R_0	23.2	51.4	64.3
Circulation (cm^2 s^{-1})	Γ	485.19	511.22	546.66
Vortex impulse (Ns)	I	0.71	1.19	1.49

the anguilliform kinematics produced the minimal velocity fluctuation, with an r.m.s. value of 0.015 m s^{-1} during steady swimming. The carangiform kinematics had larger fluctuations of 0.03 m s^{-1}, while the thunniform had the largest fluctuations, 0.065 m s^{-1}. Combined with the aforementioned analysis, the thunniform kinematics produced the fastest speed but nevertheless had the greatest speed fluctuations.

Recall previous studies on live fish: observed results from live swimming eels (anguilliform) have revealed 4–10% speed fluctuations about the mean swimming speed. For a swimming mullet, a typical carangiform swimmer, speed fluctuations of more than 20% have been observed [1]. To the best of our knowledge, there are no previous reports of swimming speed fluctuations in tuna; therefore, we cannot compare the speed fluctuations of the thunniform kinematics with that of a live specimen. The current results are in accordance to Tytell and Borazjani's recent computational results, which reported that swimming eels produce a thrust force more smoothly than swimming mackerel. By fixing the body shape and varying the kinematics, distinct speed fluctuation results are observed, possibly explained by the fact that the lift-based mechanism (which is employed by the carangiform and thunniform kinematics) inherently generates larger pressure variations than the undulatory pump mechanism (anguilliform kinematics) [24].

3.2. Power consumption of the self-propelled robotic fish

The fluid power consumption measurements for the undulation of the robotic fish's body agree well with the power estimations of live fish and the calculated results of Rome *et al* [40], who experimentally and theoretically estimated the power consumed by the muscles of live fish. As seen in figure 8, the anterior part (the first joint) took about 12% of the total power, the middle part (the second joint) took 60% and the posterior part (the last two joints) 25% of the average total hydrodynamic power for the three kinematics. Unlike the pure fluid power, the mechanical power loss gradually increased from the anterior to the posterior body. The power distribution results we obtained might also shed light on the engineering design of the robotic fish: different actuators should be selected

to provide appropriate power for the corresponding locations along the axial direction of the robotic model.

As for the fluid power coefficients reported in table 2, Borazjani and Sotiropoulos [24] used the same method to non-dimensionalize the power (i.e. dimensionalized by $\rho U^3 L^2$ as indicated in (19)), and computed a power coefficient of 0.0136 at a *Re* number of 4000, and 3.95 × 10^{-4} under inviscid conditions (i.e. $Re = \infty$, where ∞ denotes infinite). The present experiment resulted in a power coefficient of 3.39 × 10^{-3} at a *Re* number of 128 000 for carangiform kinematics. As indicated by Barrett *et al* [7] and Borazjani and Sotiropoulos [23, 24], the power coefficient decreases as the *Re* number increases; therefore, the quantities obtained from the current experiment are quite reasonable. The carangiform kinematics has a higher power coefficient than the other two modes, while the thunniform kinematics has the minimum power coefficient. Tytell [1] reported that a swimming rainbow trout (*Oncorhynchus mykiss*) has a larger estimated wake power than of an American eel, which is in accordance with the present results. In short, the present experiment shows that thunniform kinematics results in a smaller power coefficient than the other two types of undulatory kinematics.

3.3. Flow field and wake structure

In this section we describe the flow field and the wake structure generated by the robotic swimmer. Figures 9–11 showed the DPIV results of the flow field generated by the robotic swimmer with anguilliform, carangiform and thunniform kinematics, respectively. The time series of the flow field at the steady swimming state for anguilliform kinematics were demonstrated in figure 9. It can be observed that within one flapping cycle, the tail performed a flick to its right side and then another to its left, and each flick of the tail generated a vortex ring. As shown in figure 9(*b*), vortices 1 and 2 were generated from the leftward (toward the left) flick and formed the vortex ring *R1*, which is denoted by the dashed red ellipse. In figure 9(*d*), vortices 3 and 4 were generated from the rightward (toward the right) flick and formed the vortex ring *R2*. The vortex rings *R1* and *R2* are characterized by lateral divergence and then spread away from the body axis in a wedge-like arrangement. Considering the large-scale
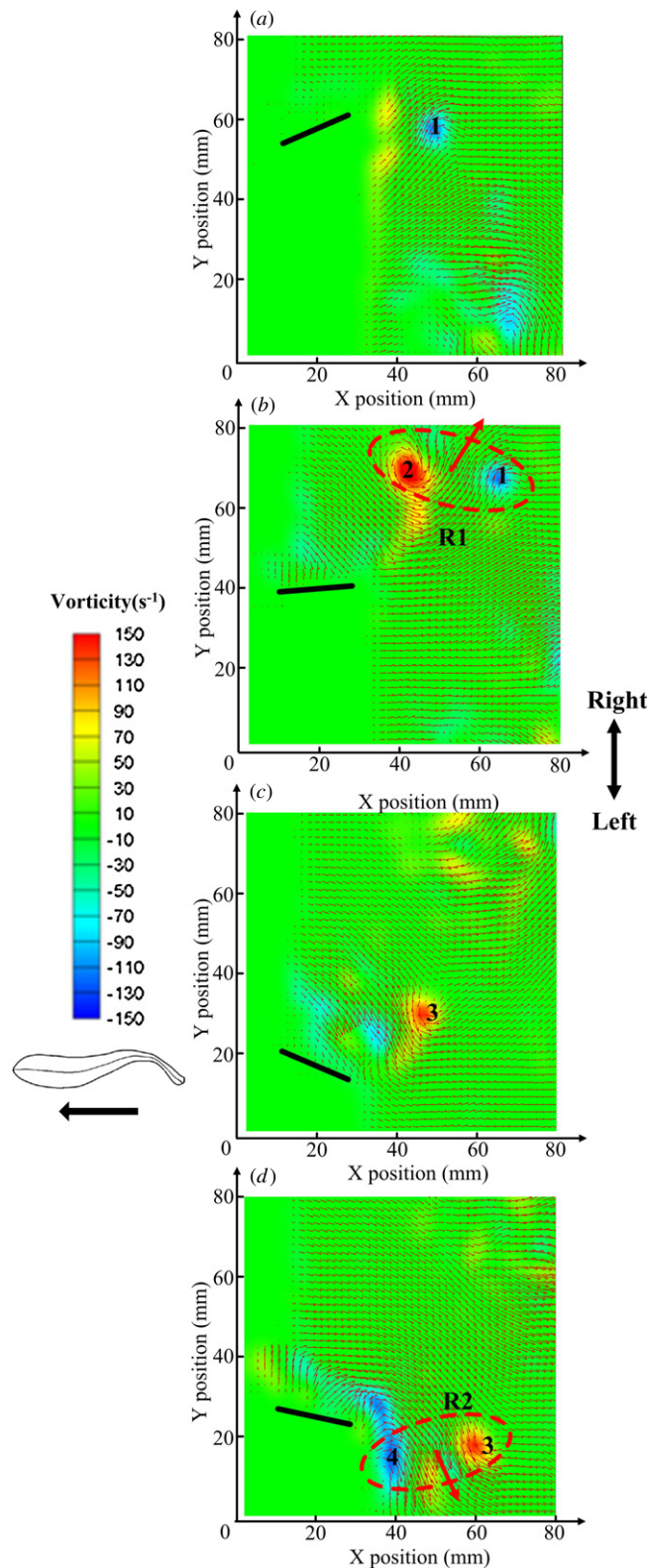
Figure 9. A double-row wake flow generated by the robotic swimmer using anguillform kinematics, where the dark drawn line indicates the position of the robotic fish's caudal fin. (*a*)–(*d*) The evolution of vorticity and flow vector fields at four different times of a flapping period: $T/4$, $T/2$, $3T/4$ and T, respectively. The direction of left and right flicks of the caudal fin is indicated by the bi-directional arrow.

characteristics of the wake structure, this type of flow field is dubbed 'double-row street' and has previously been observed in the study of the finite flapping foils by Buchholz and Smits [37]. Additionally, the wake structure is also very similar to that of a swimming eel by Tytell and Lauder [13].

The large-scale characteristics of the flow pattern generated by the robotic swimmer with carangiform kinematics (as shown in figure 10) showed no significant difference with the wake structure produced by the anguilliform kinematics. In comparison, the wake structure generated by the robotic swimmer that used thunniform kinematics varied significantly with the double-row wake. As shown in figure 11, in the case of thunniform kinematics, the vortices were organized into a single-row structure, with only one vortex ring generated per flapping beat. With carangiform and anguilliform kinematics, the two sets of vortices were located on different sides of the robotic fish's body axis, and moved backwards. Combined with previous discussions on infinite flapping foils [37, 38], this wake structure can be dubbed the conventional 'reverse Karman street'. An interesting result is that most flow visualization tests of previous robotic fish resulted in double-row wake structures [19, 21]. However, the wake pattern generated by the live carangiform fish always showed a single-row [32]. The double-row wake has seldom been observed and reported experimentally for a live adult carangiform swimmer.

Considering the differences between the wake structures of robotic and live swimmers, the present experiment employed a robotic swimmer with nearly the same body shape and kinematics (carangiform) as that of a live mackerel. Why is there still a disparity? Recent computational and experimental studies on live fish indicate that among all the factors (including the *Re* number effect, body shape, kinematics and *St*), the *St* is the primary determinant of the overall wake structure. Noting that our experiment resulted in an *St* ranging between 0.424 and 0.55, the carangiform swimmers in nature swim at an *St* within the range of 0.25–0.35 [41], which indicates that the self-propelled speed of the robotic fish is lower than that of a live fish. Although significant engineering efforts have been devoted to improving the similarity between the robotic fish and its live counterparts, a possible explanation for the *St* disparity may be due to an inherent difference in the skin material, body and fin flexure stiffness. The dependence of the wake structure on the *St* can be viewed as the ratio of the average caudal fin heave velocity to the axial forward swimming speed. So, if a self-propelled robotic fish travels at a higher *St*, the shedding vortices from the caudal fin tend to have a larger velocity component, which advects them away from the midline of the body and causes them to spread in the lateral direction. Therefore, the wake splits laterally and the double row pattern emerges—not a single-row wake.

Can the difference in wake structure be solely attributed to the effect of *St*? As can be seen from table 2, the *St* results were quite similar for the carangiform and thunniform kinematics. However, the wake structures produced by the two kinematics differ significantly. Recall that the fish's caudal fin behaves just like pitching and heaving foils, with both
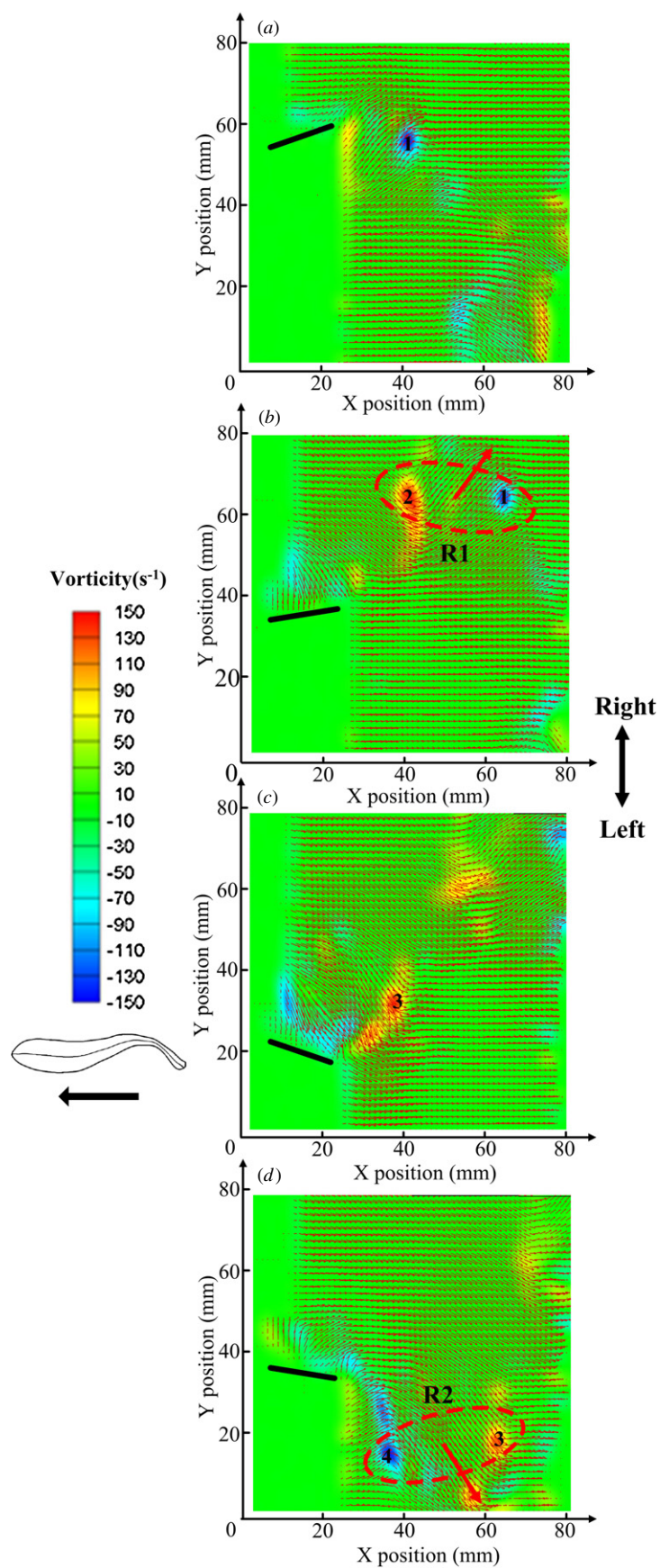
Figure 10. The double-row wake flow generated by the robotic swimmer using carangiform kinematics.
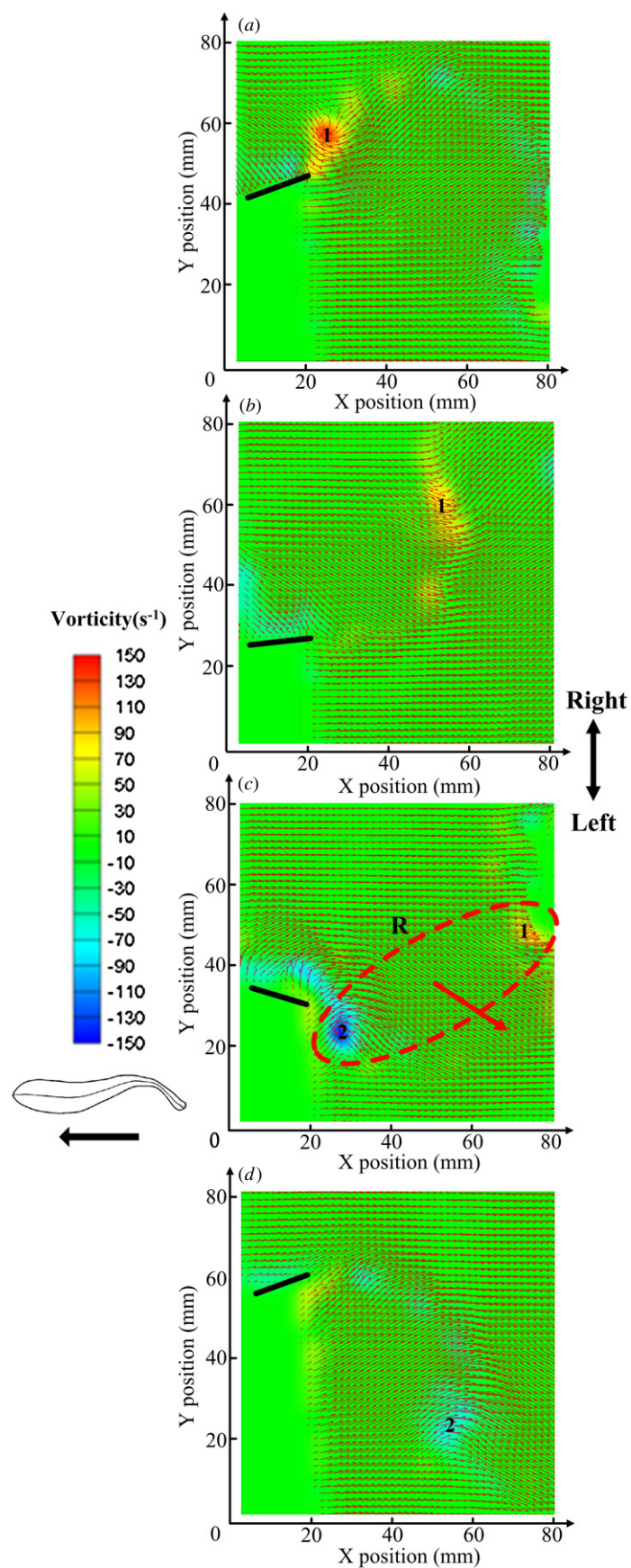
Figure 11. The single-row reverse Karman wake flow generated by the robotic swimmer using thunniform kinematics.

Table 3. The thrust efficiency results and comparisons.

Variable	Anguilliform	Carangiform	Thunniform	Finite foil	CFD-1	CFD-2
St	0.55	0.43	0.424	0.43	0.61	0.25
Aspect ratio	2.68	2.68	2.68	2.38	2.68	2.68
Re (10^5)	1.005	1.28	1.29	3.2×10^4	4×10^3	∞
η (%)	26.6	31.4	47.3	22	22.5	45

motions together determining the angle of attack, calculated as $\alpha(t) = \text{arctg}[h(t)/U] - \theta(t)$. According to the definition of the three kinematics, although the heave amplitude h and self-propelled swimming speed U are very approximate, the pitch angles for carangiform and thunniform kinematics are different. Therefore, the two kinematics result in different angles of attack α. The fin's angle of attack determines both the intensity and shedding time of the foil's leading edge vortex (LEV) [42]. Note that in this study, the angle of attack in carangiform kinematics is 1.4 times greater than that in thunniform kinematics, possibly inducing the early shed of the LEV which then interacted with the trailing edge vortex (TEV) to form a vortex ring. In comparison, as the angle of attack is relatively low, the LEV attached to the tail did not shed for the entire duration of a flapping beat and only two TEVs were generated, thereby inducing the single-row wake structure.

Besides the great dissimilarity of vortex structure between live and robotic swimmers (single row versus double row), the obvious difference is also located in the jet angle of the vortices. Wu *et al* [29] observed in a carp (*Cyprinus Carpio*, a carangiform swimmer) that the jet angle between the vortices is perpendicular to the vortex system, and points away from the fish at an angle of 36°. Obviously, much greater jet angles were produced by vortices of the present three kinematic movements on the robotic swimmer, and less energy was used by the robotic swimmer for axial thrust. As Bainbridge [31] and Wu *et al* [29] suggest, proper jet angle control by the caudal fin may be a significant factor in determining the magnitude of thrust, another possible reason for the unsatisfactory thrust performance of the present robotic fish compared to that of a live swimmer. Due to the great disparity in size and mass, it is difficult for us to make direct comparisons between the rest of the wake parameters of the robotic fish, including vortex ring radius R_0, circulation Γ and impulse I, and those of live fish. We list all the wake parameters in table 2.

3.4. Thrust efficiency

Taking into account the thrust efficiency as reported in table 3, we found that the final experimental thrust efficiency for the robotic fish is 47.3% for the thunniform kinematics, the most efficient among all three undulatory kinematics. In contrast, the efficiency value of the robotic fish using anguillform kinematics was the lowest, i.e. 26.6%. The value for carangiform kinematics is an intermediate between that for anguillform and thunniform kinematics. The robotic mackerel with thunniform kinematics not only reached higher velocities, but also achieved the maximum thrust efficiency among all three kinetic types. Note that in table 3, the quantitative

thrust efficiencies are given using various approaches: i.e. the flapping foil [42], three-dimensional computational fluid dynamics (3D-CFD) [15, 23] and the present experimental results of the robotic model. Fish fins have often been equated to flapping foils when considering their thrust performance during swimming, and the only existing prior results on thrust efficiency are based on infinite and finite biomimetic flapping foils. Therefore the experimental results of flapping foils of both the infinite and finite aspect ratios are also included in table 3.

We first considered the discrepancy in thrust efficiencies between biomimetic flapping foils and the robotic fish model. It should be noted that the infinite flapping foil denoted here is actually the flapping foil with a high aspect ratio (AR = 6) by Anderson *et al* [42], while the AR of the finite foil is 2.38 (very close to the aspect ratio of the robotic mackerel's caudal fin). At the self-propelled Strouhal number ($St = 0.43$), the thrust efficiency of an infinite flapping foil ($\eta = 61\%$) is higher than those of the robotic fish model and of the finite flapping foil, but the efficiency of the finite flapping foil ($\eta = 22\%$) approximates the results of the robotic fish. As indicated by Dong *et al* [43], this discrepancy may be due to the three-dimensional fluid effect: the thrust efficiency decreases as the aspect ratio decreases. Recently, the rapid development of 3D-CFD has provided a more scientific approach for calculating thrust efficiency computationally, in which the three-dimensional, viscous and unsteady flow effects can all be seriously considered. From table 3, Borazajani and Sotiropoulos [24] computed a thrust efficiency of 22% at $Re = 4000$ (denoted as CFD-1) and 45% at $Re = \infty$ (CFD-2). The present experiment resulted in a thrust efficiency of $\eta = 32.8\%$ at $Re = 1.28 \times 105$ and $St = 0.43$ for the carangiform kinematics, and $\eta = 47.3\%$ at $Re = 1.29 \times 105$ and $St = 0.424$ for the thunniform kinematics. As indicated by previous studies, the thrust efficiency η increases as Re increases. Therefore, the current experimental results are in good agreement with the results of the 3D-CFD.

To explain the effects of the three undulatory kinematics on thrust efficiency, we conceptualized undulatory swimming as the action of two waving plates [41], where the caudal fin corresponds to the downstream waving plate and the undulating body corresponds with the upstream waving plate. Both plates achieve a maximum thrust efficiency through optimizing two physical aspects: (1) adjusting for reasonable body undulation to achieve a minimal form drag; (2) actively controlling caudal fin motion to generate the maximum thrust force. Considering the first physical mechanism that might affect the form drag of the robotic fish, previous studies had proved that the traveling body wave would contribute to a decreased drag force by eliminating separation and

suppressing turbulence in undulatory swimming animals. In addition, a more recent numerical simulation carried out by Shen *et al* [44] indicated that less form drag can be obtained at a higher ratio of wave speed (denoted as δ, which is defined as the wave phase velocity V to the self-propelled swimming speed U). As reported in table 2, the thunniform kinematics used a relatively greater wavelength that might result in a larger ratio of the wave speed, where $\delta = 2.66$, thereby producing less form drag than the other two types of undulatory kinematics.

The caudal fin's pitch motion should also have a hydrodynamic impact on thrust performance. In this study, different angles of attack of the caudal fin were produced by the robotic swimmer using distinct kinematics. As indicated by previous studies on flapping foils [42], the recorded value of thrust efficiency as a function of the angle of attack α_{max} demonstrated that for $\alpha_{max} > 20°$, the thrust efficiency decreased as α_{max} increased; a similar trend was also observed in the study of a three-dimensional flapping foil. Since α_{max} for thunniform kinematics is smaller than that of the other two kinematics, this might lead to a better thrust performance of the robotic fish.

4. Discussion

4.1. Investigating fish biomechanics with self-propelled robots

Great progress has been made in understanding the mechanics of undulatory propulsion in fish, but the inability to control and precisely alter individual kinematic parameters has hampered biologists' ability to understand the fundamental mechanics of aquatic systems [16]. Mechatronics and related techniques have become increasingly important in experimental biology, offering the opportunity to focus research by creating robotic models that can easily be controlled to move with desired kinetic mechanisms [45, 46]. In this study, techniques of force-feedback control are applied to the hydrodynamic study of a laboratory robotic fish for the first time. The experimental apparatus which allows a robotic model to accelerate from rest to a steady speed under self-propelled conditions is described. In the apparatus, the robotic fish is mounted on a servo guide rail system and the towing speed is not preset but determined by the measured force acting on the body of the fish. Some previous studies have investigated hydrodynamics by using robots, but most of the robotic models did not satisfy self-propelled conditions [4, 19]. Encouraged by the potential generality of this simultaneous measurement method based on a force-feedback technique, we believe that unsteady bio-fluid dynamic experiments can be conducted using the present method, in such areas as the robotic undulatory fin [47, 48], pulsed jet propulsion [49], or other biomimetic devices [50].

The current study encountered some difficulties in making a robotic fish perform in the same manner as a live fish. Although the body shape of the robotic fish and its kinematics were designed and defined according to data from live fish, there are some engineering difficulties that remain before creating an artificial swimmer which moves in exactly the same way as its live counterpart. Besides the limited degree of freedom (DoF) of the robotic swimmer, we also observed that

the robotic fish's 'skin' slightly caved in while the fish was performing an undulatory movement, even if the silicon skin and foam had been adapted to conform to the robot's body. The above reasons caused some kinematic disparities between the live fish and the robot. Increasing the DoF of course will produce a better mimic; however, as indicated by biologists [16, 17], it might not be necessary to perfectly emulate the movement of live animals. As long as the robotic model exhibits the dynamic movements essential to the production of the forces and flow that match key features of its living counterpart, the results will have relevance to the original organism.

4.2. Hydrodynamic effects of the three typical undulatory kinematics

In this paper, thrust performance of the robotic fish is evaluated by self-propelled swimming speed (in this study, we use *St*) and thrust efficiency [1]. The Strouhal numbers of the robotic mackerel are 0.55 and 0.43, and 0.424 for auguilliform, carangiform and thunniform kinematics, respectively, which are higher than those of live fish ($0.25 < St < 0.35$). According to the definition of *St* in equation (16), the Strouhal number can be viewed as a result of the self-propelled speed of the robotic swimmer. The disparity between the *St* values for robotic and live swimmers therefore reflects the gap of swimming speeds. As the DPIV results additionally demonstrated, the large-scale characteristics of the flow patterns generated by the robotic swimmer emulating both anguilliform and carangiform kinematics were double-row wake structures—also different from those produced by live fish.

Although the Strouhal number results from the present self-propelled experiment do not perfectly match the *St* range of live swimmers, the results nevertheless shed light on fish undulatory biomechanics. Using self-propelled speed as the metric, the robotic mackerel using thunniform kinetic movement achieved a higher steady swimming speed relative to those using carangiform and anguilliform kinematics. However, the robotic fish using anguilliform kinematics initially performed better than the two using other kinematics. The estimated thrust efficiency showed that during a steady swimming state, thunniform kinematics is the most efficient, while anguilliform kinematics produces a relatively poor thrust efficiency; carangiform kinematics is an intermediate between the two.

Biologists and fluid engineers [15, 23] recently implemented a carangiform body-shaped fish in a three-dimensional computational model. By using both anguilliform and carangiform kinematics, they suggested that better thrust performance can be achieved by using the carangiform kinematics at a steady swimming state, yet a faster startup speed can be achieved by using a relatively shorter body wave (i.e. anguilliform kinematics). This is in accordance with the current self-propelled study. Additionally, it should be noted that the thunniform kinematics, which finally won the race of both speed and thrust efficiency in the present experiment, was not examined in the computational study. We provided some quantitative data to address this issue. The present findings

might also shed some light on the motion control of robotic fish: the robotic swimmer could determine proper movement patterns to achieve a better thrust performance depending on the situation in order to save power, i.e. for missions or requirements that require a fast start or efficient cruising.

5. Conclusions and future studies

We implemented a mackerel-shaped robot which is mounted on a servo towing system; it can determine its self-propelled speed by measuring the force acting upon it. The present experimental apparatus allows us to perform simultaneous measurements of power, flow field, swimming speed and thrust efficiency of the robotic fish under self-propelled condition. As such, we were able to pose and answer scientific questions that cannot easily be tackled experimentally with live fish. To continue exploring the hydrodynamics of fish undulatory locomotion, it is important to recognize the fact that our present work cannot conclusively determine whether the differences we found in thrust performance are due to body undulation or caudal fin movement. It is reasonable to speculate that both body undulation and caudal fin movement should play a role, but to what extent each factor contributes is not yet known. In addition to the kinetic parameters we have considered in this study, which include wavelength and caudal fin pitch angle, there are other factors that could potentially affect the wake flow and thrust efficiency of the robotic model. Systematic studies of the parametric dependence of the principal parameters on the thrust performance of robotic fish (including St, tail beat amplitude, caudal fin pitch angle and body wavelength) are very important, and will be carried out in the future.

Acknowledgments

Reference

[1] Tytell E D 2007 Do trout swim better than eels? Challenges for estimating performance based on the wake of self-propelled bodies *Exp. Fluids* **43** 701–12

[2] Webb P W 1984 Body form, locomotion and foraging in aquatic vertebrates *J. Integr. Comp. Biol.* **24** 107–20

[3] Breder C M 1926 *The Locomotion of Fishes* vol 4 (New York: New York Zoological Society) pp 159–256

[4] Hultmark M, Leftwich M and Smits A J 2007 Flow field measurements in the wake of a robotic lamprey *Exp. Fluids* **43** 683–90

[5] Yu J, Tan M, Wang S and Chen E 2004 Development of a biomimetics robotic fish and its control algorithm *IEEE Trans. Syst. Man Cybern.* B **34** 1798–810

[6] Brenden P E, Pablo V A, Kamal Y-T and Techet A H 2009 Swimming performance of a biomimetic compliant fish-like robot *Exp. Fluids* **47** 927–39

[7] Barrett D S, Triantafyllou M S and Yue D P 1999 Drag reduction in fish-like locomotion *J. Fluid Mech.* **392** 183–212

[8] Anderson J M and Chhabra N 2002 Maneuvering and stability performance of a robotic tuna *J. Integr. Comp. Biol.* **42** 118–26

[9] Hu H, Liu J D and Francis G 2006 Design of 3D swim patterns for autonomous robotic fish *Proc. IEEE/RSJ Int. Conf. on Intelligent Robots and Systems* pp 2406–11

[10] Wang T M, Wen L, Liang J H and Wu G H 2010 Fuzzy vorticity control of a biomimetic robotic fish using a flapping lunate tail *J. Bionic. Eng.* **7** 56–65

[11] Liao J 2002 Swimming in needlefish (Belonidae): anguilliform locomotion with fins *J. Exp. Biol.* **205** 2875–84

[12] Lighthill M J 1971 Large-amplitude elongated-body theory of fish locomotion *Proc. R. Soc. Lond.* B **179** 125–38

[13] Tytell E D and Lauder G V 2004 The hydrodynamics of eel swimming: I. Wake structure *J. Exp. Biol.* **207** 1825–41

[14] Wilga C D and Lauder G V 2004 Hydrodynamic function of the shark's tail *Nature* **430** 850

[15] Tytell E D, Borazjani I, Sotiropoulos F, Baker T V, Anderson E J and Lauder G V 2010 Disentangling the functional roles of morphology and motion in the swimming of fish *J. Integr. Comp. Biol.* **50** 1140–56

[16] Lauder G V 2011 Swimming hydrodynamics: ten questions and the technical approaches needed to resolve them *Exp. Fluids* **51** 23–35

[17] Lauder G V *et al* 2007 Fish biorobotics: kinematics and hydrodynamics of self-propulsion *J. Exp. Biol.* **210** 2767–80

[18] Low K H and Chong C W 2010 Parametric study of the swimming performance of a fish robot propelled by a flexible caudal fin *Bioinspir. Biomim.* **5** 1–9

[19] Tan G K, Shen G X, Huang S Q, Su W H and Ke Y 2007 Investigation of flow mechanism of a robotic fish swimming by using flow visualization synchronized with hydrodynamic force measurement *Exp. Fluids* **43** 811–21

[20] Beal D N and Bandyopadhyay P R 2007 A harmonic model of hydrodynamic forces produced by a flapping fin *Exp. Fluids* **43** 675–82

[21] Brücker C and Bleckmann H 2007 Vortex dynamics in the wake of a mechanical fish *Exp. Fluids* **43** 799–810

[22] Candelier F, Boyer F and Leroyer A 2011 Three-dimensional extension of Lighthill's large-amplitude elongated-body theory of fish locomotion *J. Fluid Mech.* **674** 196–226

[23] Borazjani I and Sotiropoulos F 2010 On the role of form and kinematics on the hydrodynamics of self-propelled fish *J. Exp. Biol.* **213** 89–107

[24] Borazjani I and Sotiropoulos F 2008 Numerical investigation of the hydrodynamics of carangiform swimming in the transitional and inertial flow regimes *J. Exp. Biol.* **211** 1541–58

[25] Tytell E D, Hsu C Y, Williams T L, Cohen A H and Fauci L J 2010 Interactions between body stiffness, muscle activation, and fluid environment in a neuromechanical model of lamprey swimming *Proc. Natl Acad. Sci. USA* **107** 19832–7

[26] Stefan K and Koumoutsakos P 2006 Simulations of optimized anguilliform swimming *J. Exp. Biol.* **209** 4841–57

[27] Mori N and Chang K Introduction to MPIV–PIV toolbox in MATLAB- version 0.965 [EB/OL]. 2004-12-21 http://sauron.urban.eng.osaka-cu.ac.jp/~mori/softwares/mpiv.

[28] Wen L, Wang T M, Liang J H and Wu G H 2011 A novel method based on a force-feedback technique for the hydrodynamic investigation of kinematics effects on robotic fish *Proc. IEEE Int. Conf. Robotics and Automation* pp 203–8

[29] Wu G, Yang Y and Zeng L 2007 Kinematics, hydrodynamics and energetic advantages of burst-and-coast swimming of koi carps (Cyprinus carpio koi) *J. Exp. Biol.* **210** 2181–91

[30] Shadwick R E and Lauder G V 2006 *Fish Biomechanics* vol 23 (Amsterdam: Elsevier) pp 426–9

[31] Bainbridge R 1963 Caudal fin and body movements in the propulsion of some fish *J. Exp. Biol.* **40** 23–56

[32] Fish F E and Lauder G V 2006 Passive and active flow control by swimming fishes and mammals *Annu. Rev. Fluid Mech.* **38** 193–224

[33] Hess F and Videler J J 1984 Fast continuous swimming of Saithe (Pollachius Virens): a dynamic analysis of bending moments and muscle power *J. Exp. Biol.* **109** 229–51

[34] Donley J M and Dickson K A 2000 Swimming kinematics of juvenile kawakawa tuna (Euthynnus affinis) and chub mackerel (Scomber japonicus) *J. Exp. Biol.* **203** 3103–16

[35] Dewar H and Graham J 1994 Studies of tropical tuna swimming performance in a large water tunnel *J. Exp. Biol.* **192** 45–59

[36] Cheng J-Y and Blickhan R 1994 Note on the calculation of propeller efficiency using elongated body theory *J. Exp. Biol.* **192** 169–77

[37] Buchholz J H and Smits A J 2008 The wake structure and thrust performance of a rigid low-aspect-ratio pitching panel *J. Fluid Mech.* **603** 331–65

[38] Triantyfyllou M S and Triantyfyllou G S 1995 An efficient swimming machine *Sci. Am.* **272** 64–71

[39] Blake R W and Domenici 2000 *Biomechanics in Animal Behavior* (Oxford: BIOS Scientific)

[40] Rome L C, Swank D and Corda D 1993 How fish power swimming *Science* **261** 340–3

[41] Triantafyllou M S 2005 Review of hydrodynamic scaling laws in aquatic locomotion and fish-like swimming *Appl. Mech. Rev.* **58** 226–38

[42] Anderson J M, Streitlien K and Barrett D S 1998 Oscillating foils of high propulsive efficiency *J. Fluid Mech.* **360** 41–72

[43] Dong H, Mittal R and Najjar F 2006 Wake topology and hydrodynamic performance of low aspect-ratio flapping foils *J. Fluid Mech.* **566** 309–43

[44] Shen L, Zhang X, Yue D P and Triantafyllou M S 2003 Turbulent flow over a flexible wall undergoing a streamwise traveling wave motion *J. Fluid Mech.* **484** 197–221

[45] Blake R W 2010 Special issue on the biomimetics of aquatic lift: applications for engineering *Bioinspir. Biomim.* **5** 3

[46] Low K H 2009 Preface: Why biomimetics? *Mech. Mach. Theory* **44** 511–2

[47] Oscar M C, Neelesh A P, Lauder G V and MacIver M 2011 Mechanical properties of a bio-inspired robotic knifefish with an undulatory propulsor *Bioinspir. Biomim.* **6** 026004

[48] Low K H 2009 Modeling and parametric study of modular undulating fin rays for fish robots *Mech. Mach. Theory* **44** 615–32

[49] Moslemi A and Krueger P 2010 Propulsive efficiency of a biomorphic pulsed-jet underwater vehicle *Bioinspir. Biomim.* **5** 036003

[50] Jordi C, Michel S and Fink E 2010 Fish-like propulsion of an airship with planar membrane electric elastomer actuators *Bioinspir. Biomim.* **5** 026007